Low-Power Design of a Self-powered Piezoelectric Energy Harvesting System With Maximum Power Point Tracking

Na Kong, *Student Member, IEEE*, and Dong Sam Ha, *Fellow, IEEE*

Abstract—A low-power energy harvesting system targeting to harvest several milliwatts from vibration is presented in this paper. Several low-power design schemes to reduce power dissipation of the proposed system are described, and sources of power loss are analyzed to improve the power efficiency. A discontinuous conduction mode (DCM) flyback converter with the constant on-time modulation is adopted for our system. The DCM operation of a flyback converter is chosen as for maximum power point tracking (MPPT) to be implemented with a single current sensor. The constant on-time modulation lowers the clock frequency of the controller by more than an order of magnitude for our system, which reduces the dynamic power dissipation of the controller. MPPT, executed by a microcontroller unit (MCU), is achieved through dynamic resistive matching, and the MPPT is executed at intermittent time intervals due to a relatively slow change of the operating condition. When MPPT is not active, the MCU operates at a lower clock frequency to save power. Experimental results indicate that the proposed system harvests up to 8.4 mW power under 0.5-g base acceleration with four parallel piezoelectric cantilevers and achieves 72% power efficiency around the resonant frequency of 47 Hz.

Index Terms—Impedance matching, piezoelectric transducers, power conditioning, power conversion, pulse frequency modulation.

I. INTRODUCTION

WIRELESS sensor nodes (WSNs) have been pervasive in the past decade and used in various applications such as industrial process monitoring, healthcare, home automation, and structural health monitoring. However, the batteries used to power WSNs have become a major bottleneck for wide deployment. The power required for WSNs may range from a few microwatts to hundreds of milliwatts. Extensive research has been conducted to reduce the power dissipation of WSNs through various means, including exploitation of low duty cycles and low-power design of sensors, circuits, and systems. Another avenue taken to address the problem is energy harvesting from ambient sources such as solar, wind, vibration, heat and radio frequency radiation [1]–[7]. This paper considers harvesting vibration energy for WSNs using piezoelectric cantilevers as the transducer due to its relatively higher power density [8]–[10].

Design of power management (PM) circuits to harvest maximal energy from piezoelectric patches has been investigated rather intensively in recent years [11]–[22]. The key underlying scheme for those works is impedance matching between the load and the source. Two major technical challenges for the circuit design are 1) a piezoelectric patch exhibits large capacitance, and a rudimentary approach requires an impractical size inductor on the load; and 2) the source impedance changes as the environmental condition changes. Existing works can be classified into two groups based on the impedance matching methods employed, conjugate matching and resistive matching. The first group intends to achieve the conjugate matching with nonlinear treatments. They use MOSFETs and off-the-shelf inductors to shape the output voltage and current waveform, equivalently change the load impedance [11]–[17]. This method has potential to offer a higher power transfer for a wider range of vibration frequency than resistive matching. However, since MOSFETs should be switched synchronously with the displacement of the cantilever beam, it is challenging to realize stringent timing control with reasonably low circuit complexity and low power consumption [15], [16].

The second group of works attempts to realize resistive matching [18]–[22]. The rationale behind resistive matching is that the impedance of a piezoelectric cantilever vibrating around the resonant frequency is mostly resistive. The PM circuit in [18] utilizes a dc–dc buck converter to realize dynamic resistive matching through adjustment of the duty cycle. The circuit employs a DSP-based controller powered by an external power source, and the controller consumes more power than it can harvest from a typical size piezoelectric cantilever. Later, in order to reduce power dissipation, the processor is replaced with discrete components and the converter runs at a fixed duty cycle, while giving up dynamic resistive matching [19]. The controller dissipates around 5.74-mW power, which is far less than a DSP-based controller, but still excessive for the intended application. The self-powered management circuits in [21] and [22] give up dynamic impedance matching in favor of power reduction of the driving circuit to several microwatts. Absence of dynamic impedance matching results in low efficiency due to changing operating conditions.

Another important requirement of a PM circuit for energy harvesting is the ability to cold start. A rudimentary solution
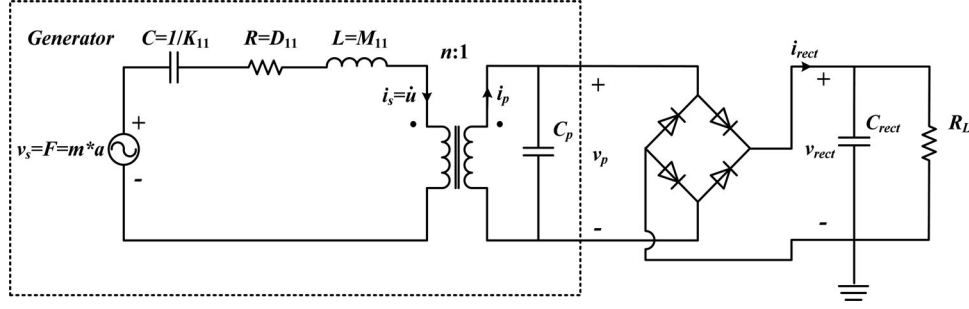
Fig. 1.   Piezoelectric generator model with an AC–DC rectifier and load.

is to include a precharged battery, as adopted by most existing self-powered energy harvesting systems [14]–[17], [23]–[25]. However, if the battery of such a system is discharged completely, the system fails to self-start. To our knowledge, existing PM circuits capable of dynamic impedance or resistive matching have not addressed the start-up problem.

In this paper, we present a low-power PM system for piezoelectric energy harvesting. The proposed system adopts dynamic resistive matching and is able to cold start without relying on a backup battery. A discontinuous conduction mode (DCM) flyback converter with the constant on-time modulation is employed for the power stage. A low-power microcontroller unit (MCU) is programmed to perform the maximum power point tracking (MPPT) to maximize energy harvesting. The MCU usually already exists in a WSN. Therefore, the use of MCU does not require extra hardware. The low-power design features presented in this paper can readily be applied to other types of energy harvesting systems such as small scale wind turbines and solar panels.

This paper is organized as follows. Section II reviews the characteristics of piezoelectric harvesters. Section III presents the overview of the proposed system and describes low-power design schemes employed for our system. It also analyzes sources of power loss and presents efficiency metrics. Section IV presents the experimental results including the system performance and a breakdown of the power loss. Section V concludes the paper.

II. CHARACTERISTICS OF THE PIEZOELECTRIC ENERGY HARVESTER

A piezoelectric energy harvester is typically a cantilevered beam with one or two piezoceramic layers (a unimorph or bimorph). The equivalent circuit for the first vibrational mode of a bimorph piezoelectric cantilever is shown in Fig. 1 [26]. The voltage generator $v = m^*a$ represents the force induced by the base vibration, where m^* is the effective modal forcing term and a is the base acceleration. The current i_S out of the voltage source v is the velocity of the tip mass at the end of the beam along three-axis, i.e., the derivative of the displacement of the tip mass u. The equivalent inductor $L = M_{11}$ represents the modal mass of the first mode. The resistor $R = D_{11}$ and the capacitor $C = 1/K_{11}$ represent mechanical damping and compliance (reciprocal of stiffness), respectively. The electromechanical coupling
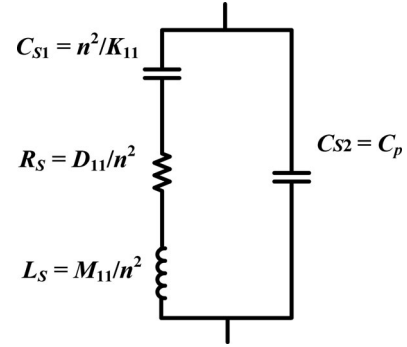

Fig. 2.   Equivalent source impedance of a piezoelectric generator.

M_{11}	D_{11}	K_{11}	n	C_P	m^*
1	15.50671	82461.67	-0.01964044	41.24e-9	0.1286161

is modeled as a transformer with the turns ratio of n. C_P is the equivalent inherent capacitance of the piezoceramic layers.

The impedance z_S of the piezoelectric cantilever generator can be represented as shown in Fig. 2, where

$$L_S = \frac{L}{n^2} = \frac{M_{11}}{n^2}, \qquad R_S = \frac{R}{n^2} = \frac{D_{11}}{n^2},$$

$$C_{S1} = n^2 C = \frac{n^2}{K_{11}}, \qquad C_{S2} = C_p. \qquad (1)$$

In order to understand the property of the source impedance, the parameters of a bimorph piezoelectric generator used in [27] are listed in Table I. The same type of the piezoelectric cantilever is used for our experiment. The bimorph (model number T226-A4-503X of Piezo Systems, Inc., Woburn, MA) consists of two opposite-poled PZT-5 A piezoelectric elements bracketing a brass substructure layer, and the two piezoelectric elements are connected in series internally. The impedance of the generator is plotted in Fig. 3.

Fig. 3 shows that the source impedance becomes purely resistive around the resonance frequency 47 Hz and becomes capacitive for frequencies off from the resonance. Hence, resistive load matching extracts the maximum power at the resonance. The piezoelectric generator for our experiment is shown in Fig. 4,
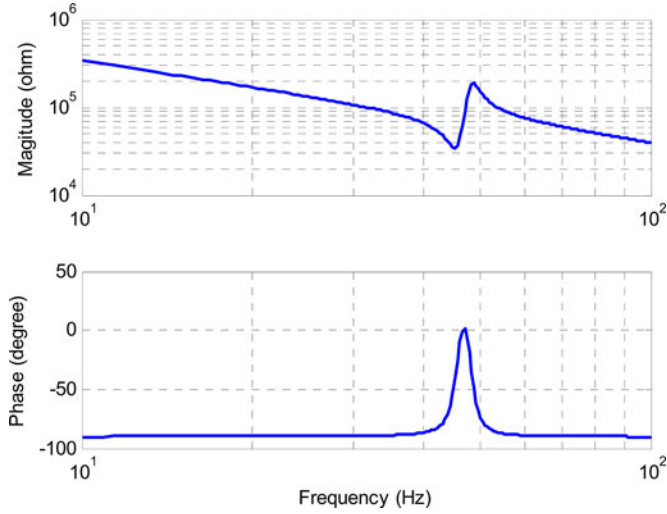
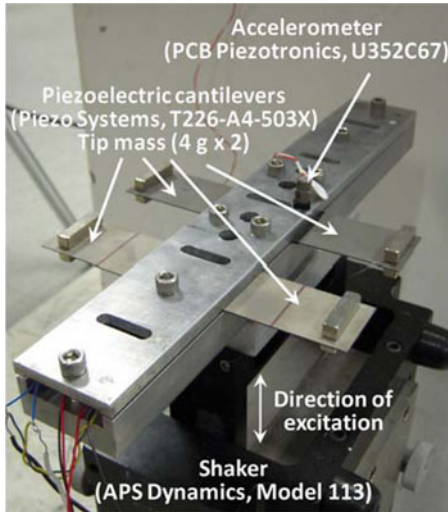Fig. 3. Source impedance of a bimorph piezoelectric harvester.

Fig. 5. Optimal load resistance.

Fig. 4. Cantilevered bimorph generator.

Fig. 6. Diagram of the proposed system.

A. System Diagram and its Operation

Fig. 6 shows a diagram of the proposed PM system, which intends to illustrate the system operation (instead of the actual implementation). The system adopts a flyback converter, which is able to step up or down the input voltage. A 5-V supercapacitor is chosen as the energy storage device due to its virtually unlimited life cycles and simple charge mechanism. Linear Regulator 1 and the oscillator in Fig. 6 are responsible for the start-up. A low-power MCU MSP430 from Texas Instruments implements an MPPT algorithm. Linear Regulator 2 regulates supercapacitor's voltage to 3 V to power up the MCU.

B. Low-Power Design Schemes

Low power dissipation is the key design objective for the proposed PM system. All design choices including the circuit topology are made judiciously to reduce the overall power dissipation without an excessive sacrifice on the performance. A few major design choices are described in the following.

DCM Flyback Converter: A buck-boost converter is able to handle a wide range of the input voltage, below or above the output voltage. DCM buck-boost converter behaves as a lossless resistor [28]. These two features make the buck-boost converter a popular choice for piezoelectric energy harvesting [20]–[22]. To apply an MPPT algorithm, a controller needs to know the

which has four bimorph cantilevers connected in parallel. Two 4-g magnets attached to the tip of each cantilever increase the effective mass and enable us to tune the resonant frequency of the beam. The resonant frequencies of each cantilever are tuned to be the same at around 47 Hz. The optimal resistive load around the resonant frequency was identified by tuning the load manually. The optimal resistor ranges from 10 to 50 kΩ as shown in Fig. 5.

III. PROPOSED PM SYSTEM

The proposed PM system for piezoelectric energy harvesting adopts a flyback converter with the constant on-time modulation for dynamic resistive matching. The operation of the system, low-power design schemes, and the start-up feature employed are described in this section.
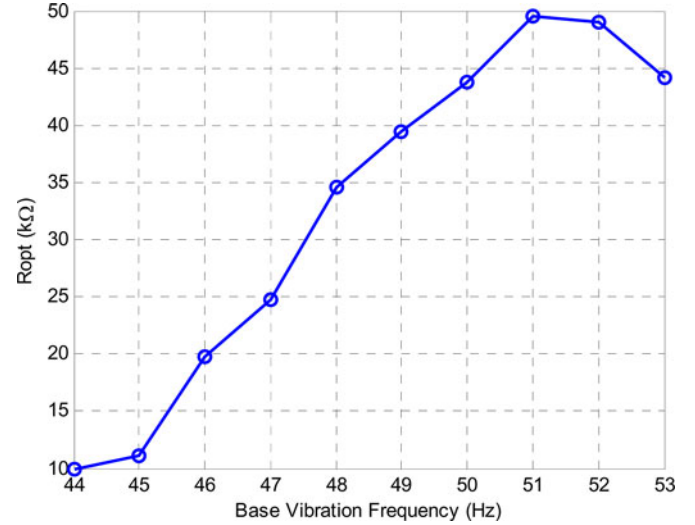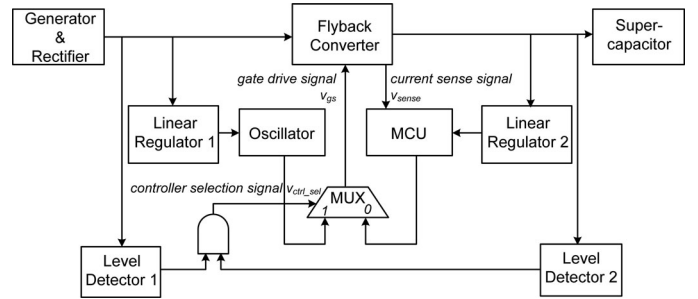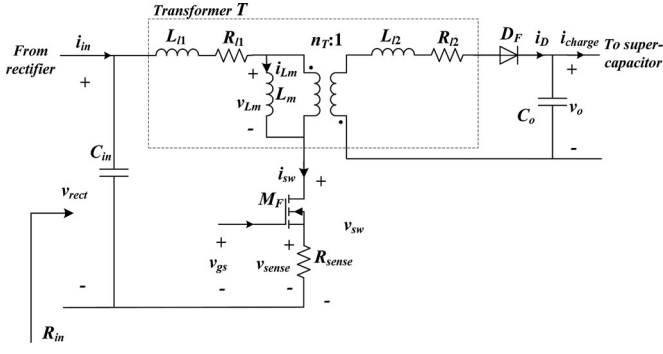
Fig. 7. Circuit diagram of the flyback converter.

average harvested power, which typically requires sensing both the voltage and the current. However, the power information of a DCM buck–boost converter can be obtained by sensing only the inductor current, which saves power associated with the sensing. The feature is analyzed in detail as follows.

The derivative of a buck–boost converter, flyback converter, is adopted for our system owing to the noninverting output voltage and the relative low circuit complexity compared to other buck–boost type converters such as single-ended primary-inductor converter. The circuit diagram of a flyback converter is shown in Fig. 7, and the voltage and current waveforms are shown in Fig. 8. For simplicity, the MOSFET, diode, and transformer are assumed lossless, and detailed loss analysis is given in Section III-C. Magnetizing inductance L_m functions in the same manner as the inductor in a traditional buck–boost converter. The magnetizing current for one switching cycle is obtained as follows:

$$i_{Lm}(t) = \begin{cases} \dfrac{v_{\text{rect}}}{L_m}t, & 0 < t \le d_1 T_s \\ \dfrac{V_{\text{rect}}d_1 T_s}{L_m} - \dfrac{n_T v_o}{L_m}(t - d_1 T_s), & d_1 T_s < t \le (d_1 + d_2)T_s \\ 0, & (d_1 + d_2)T_s < t \le T_s. \end{cases}$$

(2)

The effective input resistance R_{in} of the flyback converter is obtained as (3) [28]. The input resistance is a function of the duty cycle d_1 and the switching period T_s, or the switch ON-time, rather than the input or output voltages of the converter

$$R_{\text{in}} = \frac{v_{\text{rect}}}{\frac{1}{T_S}\int_0^{d_1 T_S} i_{Lm}dt} = \frac{v_{\text{rect}}}{\frac{1}{T_S}\int_0^{d_1 T_S} \frac{v_{\text{rect}}}{L_m}t\,dt}$$
$$= \frac{2L_m}{d_1^2 T_s} = \frac{2L_m T_s}{T_{\text{on}}^2}.$$

(3)

The effective input resistance R_{in} should be equal to the source impedance of the piezoelectric cantilever $R_{\text{in,opt}}$ for resistive matching.

The inductor current reaches its peak $i_{Lm,\max}$ at the end of each switch ON-time and releases the inductor energy completely to the load during the switch OFF-time due to the DCM operation. The average power delivered to the load for each
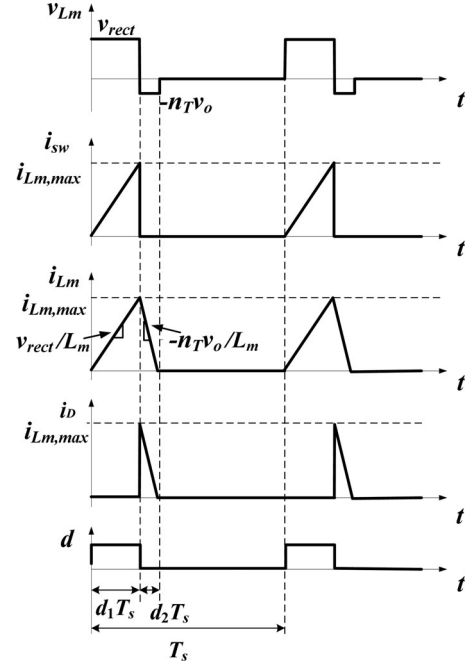

Fig. 8. Waveforms in a switching cycle.

switching cycle can be expressed as

$$P_{\text{avg}} = \frac{L_m i_{Lm,\max}^2}{2T_s}.$$

(4)

Therefore, by sensing only the inductor current through the sensing resistor R_{sense} in Fig. 7, the controller is able to compute the average power delivered to the converter, which simplifies the sensing circuit and the MPPT algorithm to save power.

Constant On-Time Modulation: Power consumption of the controller for our system is mainly due to the dynamic power dissipation of the MCU, which is proportional to the MCU clock frequency. The clock frequency is determined by the resolution of the duty cycle that the system is required to achieve [29]. In order to realize MPPT (which implements the hill-climbing algorithm [30], [31]) for the proposed system, it adjusts the duty cycle, which in turn changes the input resistance of the converter. Therefore, the required resolution of the input resistance determines the clock frequency of the MCU. The resolution of the input resistance for the constant frequency modulation and the constant on-time modulations are given as follows:

$$\Delta R_{\text{in\_const}Fs} = \frac{2L_m T_s}{T_{\text{on}}^2} - \frac{2L_m T_s}{(T_{\text{on}} + \Delta T_{\text{on}})^2} \approx \frac{4L_m T_s \Delta T_{\text{on}}}{T_{\text{on}}^3}$$
$$= \frac{2L_m}{T_{\text{on}}^2} \cdot \frac{2}{d_1} \cdot \Delta T_{\text{on}}$$

(5)

$$\Delta R_{\text{in\_const}Ton} = \frac{2L_m T_s}{T_{\text{on}}^2} - \frac{2L_m(T_s - \Delta T_{\text{off}})}{T_{\text{on}}^2}$$
$$= \frac{2L_m}{T_{\text{on}}^2} \cdot \Delta T_{\text{off}}.$$

(6)

The aforementioned expressions reveal that, to achieve the same resolution, the constant frequency modulation requires $\frac{2}{d_1}$
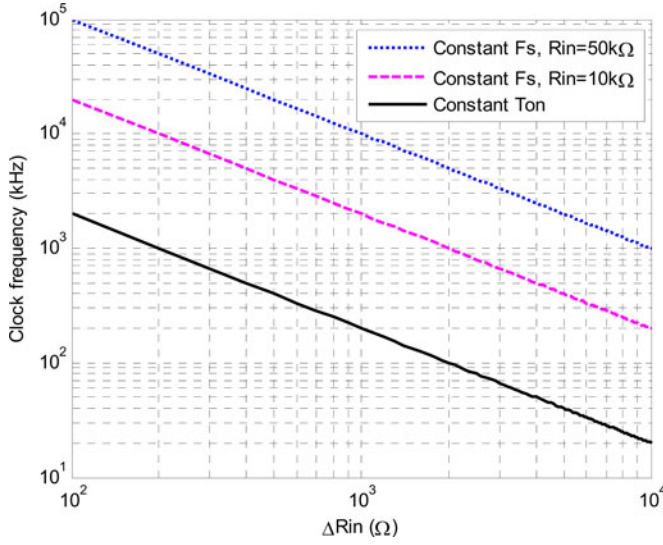
Fig. 9. Minimum clock frequency versus resolution of the input resistance.

times higher clock frequency than the constant on-time modulation. Fig. 9 shows the minimum clock frequency versus the resolution of the input resistance for the circuit used for our experiments (given in Section IV), whose parameters are $T_{\rm on} = 10~\mu{\rm s}$, $L_m = 10$ mH, $n_T = 1$, and $R_{\rm in,opt} = 10$–50 kΩ. The required clock frequency for the constant on-time modulation is reduced by a factor of 10–50 times compared to the constant frequency modulation, which in turn reduces the power consumption of the MCU.

Under the constant on-time modulation, the hill-climbing MPPT algorithm operates as follows. The current switching period is decreased with a predetermined step. The inductor current is sampled at the middle of the switch ON-time (to avoid the noisy peak current), and the controller calculates the average power using (4). If the average input power increases, the switching period is decreased again with the same predetermined step size; otherwise, the switching period is increased by the same step size. The hill-climbing process continues to settle around the optimal switching period.

Switch of the MCU Clock Frequency: Since environmental conditions such as temperature and vibration frequency change relatively slow compared with the processor speed, the MPPT algorithm is performed periodically to save power. For the proposed system, the MCU executes the MPPT algorithm for 20 ms at 8-MHz clock frequency and is in sleep mode at 1-MHz clock frequency for the following 2 s. The MCU maintains the current duty cycle in the sleep mode. Fig. 10 shows the current profile of the MCU with the supply voltage of 3 V. It consumes 7.8 mW (with its current 2.6 mA) in the active mode and 330 μW (with its current 110 μA) during the sleep mode, which results in the average MCU power of 408 μW during the operation.

C. Loss Breakdown of a Flyback Converter

We analyze the sources of power dissipation for the flyback converter, in order to select adequate circuit components and improve the efficiency. We assume that the converter runs

at a steady state, in which the resistive matching has already been achieved. Under this assumption, the major power loss is due to power dissipation of four components—MOSFET M_F, transformer T, diode D_F, and sensing resistor $R_{\rm sense}$. Refer to Figs. 7 and 8 for notations used for the expressions given in the following.

MOSFET M_F: The loss associated with MOSFET M_F is mainly the conduction loss and switching loss. The conduction loss is due to the channel on-resistance $R_{\rm ds,on}$ and occurs during the switch ON-time. It can be obtained as

$$P_{\rm MOSFET,cond} = \frac{1}{T_s} \int_0^{d_1 T_s} i_{Lm}^2 R_{\rm ds,on} dt$$

$$= \frac{1}{T_s} \int_0^{d_1 T_s} \left(\frac{i_{Lm,\max}}{d_1 T_S} t \right)^2 R_{\rm ds,on} dt$$

$$= \frac{1}{3} \left(i_{Lm,\max} \right)^2 d_1 R_{\rm ds,on} \qquad (7)$$

where the maximum inductor $i_{\rm Lm,max}$ is approximately

$$i_{Lm,\max} = \frac{V_{\rm rect} T_{\rm on}}{L_m}. \qquad (8)$$

Substituting (3) and (8) into (7) leads to

$$P_{\rm MOSFET,cond} = \frac{2V_{\rm rect}^2 T_{\rm on} R_{\rm ds,on}}{3 L_m R_{\rm in,opt}}. \qquad (9)$$

The switching loss is due to the voltage–current overlap during the turn-OFF transition and the loss on output capacitance during the turn-ON transition

$$P_{\rm MOSFET,switch} = \left(\frac{1}{2} \left(V_{\rm rect} + n_T V_o \right) i_{Lm,\max} t_f \right.$$

$$\left. + \frac{1}{2} C_{\rm oss} \left(V_{\rm rect} + n_T V_o \right)^2 \right) F_s$$

$$= \left(\left(V_{\rm rect} + n_T V_o \right) \frac{V_{\rm rect} T_{\rm on}}{L_m} t_f \right.$$

$$\left. + C_{\rm oss} \left(V_{\rm rect} + n_T V_o \right)^2 \right) \frac{L_m}{T_{\rm on}^2 R_{\rm in,opt}} \qquad (10)$$

where F_s is the switching frequency, t_f is the falling time of the gate input signal, and $C_{\rm oss}$ denotes the output capacitance of the MOSFET.

Transformer T: The loss associated with the transformer is mainly due to the parasitic resistance R_{l1} and R_{l2} of the copper wires. It can be obtained as

$$P_{\rm transformer} = \frac{1}{T_s} \left[\int_0^{d_1 T_s} i_{Lm}^2 R_{l1} dt + \int_{d_1 T_s}^{T_s} \left(n_T i_{Lm} \right)^2 R_{l2} dt \right]$$

$$= \frac{1}{3} \left(i_{Lm,\max} \right)^2 \left(d_1 R_{l1} + d_2 n_T^2 R_{l2} \right) \qquad (11)$$

where d_2 is approximately

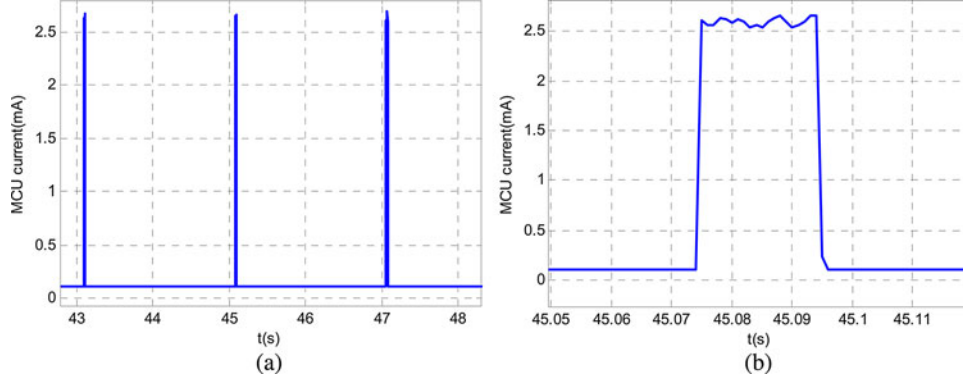$$d_2 = \frac{d_1 V_{\rm rect}}{n_T V_o}. \qquad (12)$$

Fig. 10.   Current profile of the MCU. (a) Normal view. (b) Close-up view.

Substituting (3) and (12) into (11) leads to

$$P_{\text{transformer}} = \frac{2V_{\text{rect}}^2 T_{\text{on}}}{3L_m R_{\text{in,opt}}} \left(R_{l1} + \frac{n_T V_{\text{rect}}}{V_o} R_{l2} \right). \quad (13)$$

Note that the choice of T_{on}, n_T, and L_m values should guarantee the DCM operation or meet $d_1 + d_2 < 1$.

Diode D_F: The first-order forward voltage drop of the diode is expressed as $v_F = ki_L + b$, where i_L is the forward current, k and b are constants, and the power loss of a diode is $\text{v}_F i_{\text{Lm}}$. The current flows through the diode only during the switch OFF-time. The average conduction loss of the diode is obtained as

$$
\begin{aligned}
P_{\text{diode,cond}} &= \frac{1}{T_s} \int_0^{d_2 T_s} \left(k \left(\frac{n_T i_{Lm,\max}}{d_2 T_s} t \right) + b \right) \\
&\quad \times \left(\frac{n_T i_{Lm,\max}}{d_2 T_s} t \right) dt \\
&= d_2 \left(\frac{k}{3} (n_T i_{Lm,\max})^2 + \frac{b}{2} n_T i_{Lm,\max} \right) \\
&= \frac{2k n_T V_{\text{rect}}^3 T_{\text{on}}}{3 V_o L_m R_{\text{in,opt}}} + \frac{b V_{\text{rect}}^2}{V_o R_{\text{in,opt}}}. \quad (14)
\end{aligned}
$$

The switching loss of the diode is only the loss on its junction capacitance during its turn-ON transition

$$
\begin{aligned}
P_{\text{diode,swtch}} &= \frac{1}{2} C_j \left(V_o + V_{\text{rect}}/n_T \right)^2 F_s \\
&= \frac{1}{2} C_j \left(V_o + V_{\text{rect}}/n_T \right)^2 \frac{2L_m}{T_{\text{on}}^2 R_{\text{in,opt}}} \quad (15)
\end{aligned}
$$

where C_j is the diode capacitance.

Sensing Resistor R_{sense}: Power loss due to the sensing resistor is similar to $R_{\text{ds,on}}$ of the MOSFET

$$P_{R\text{sense}} = \frac{1}{3} (i_{Lm,\max})^2 d_1 R_{\text{sense}} = \frac{2V_{\text{rect}}^2 T_{\text{on}} R_{\text{sense}}}{3L_m R_{\text{in,opt}}}. \quad (16)$$

Small R_{sense} reduces the power loss. However, small R_{sense} increases noise during the current sensing, which degrades the performance of the MPPT operation. Further, the range of the voltage drop across R_{sense} is also imposed by the ADC.

D. Metrics for Efficiency

We define the overall system efficiency η_{overall} as the ratio of the harvested power P_{out} on the supercapacitor to the power $P_{\max}$ dissipated by a perfectly matched load directly connected at the rectifier output of the piezoelectric generator (equivalently at the input of the flyback converter). The overall system efficiency is formally expressed as follows:

$$\eta_{\text{overall}} = \frac{P_{\text{out}}}{P_{\max}}. \quad (17)$$

Two sources contribute to the overall system efficiency. One source is the impedance matching performance called *MPPT efficiency* in this paper, and the other one is the power conversion performance in the flyback converter called *conversion efficiency*. The MPPT efficiency η_{MPPT} is defined as the ratio of the power P_{in} flowing into the flyback converter to the power harvested by the optimal resistor, and the conversion efficiency $\eta_{\text{conversion}}$ is the ratio of the harvested power P_{out} on the supercapacitor to the power P_{in} flowing into the flyback converter. They are defined formally as follows:

$$\eta_{\text{MPPT}} = \frac{P_{\text{in}}}{P_{\max}} \quad (18)$$

$$\eta_{\text{conversion}} = \frac{P_{\text{out}}}{P_{\text{in}}}. \quad (19)$$

Note that the overall system efficiency is the product of the two efficiency terms.

E. Start-Up Strategy

The loading of the MCU is relatively heavy to the piezoelectric generator, which only generates several milliwatts. Connection of the MCU to the source changes the input impedance of the converter and complicates the impedance matching mechanism. Therefore, the MCU should be powered by the output voltage of the converter (or the supercapacitor). Then, the problem is to start-up the MCU when the energy stored on the supercapacitor is completely drained. A low-power oscillator directly powered by the source is proposed to solve the problem, and the system starts as follows. Suppose that the supercapacitor is initially discharged. The piezoelectric generator powers up Linear Regulator 1 in Fig. 6, which in turn powers up the

TABLE II
COMPONENTS AND CIRCUIT PARAMETERS

Component	Part Number	Circuit Parameters
Rectifier	BAS3007	V_F = 0.35 V@ 100 mA
MOSFET M_F	2N7002	R_{dson} = 1.7 Ω-5.3 Ω, C_{oss}= 15 pF
Schottky Diode D_F	PMEG4005	V_F = 0.220V@10mA; 0.295V@100mA; C_j = 50 pF
Supercapacitor	GW209F	C = 0.12 F; ESR = 70 mΩ
Sensing resistor R_{sense}	--	47 Ω
Transformer T	--	L_m = 10mH; n_T =1; R_{l1} = 6Ω, R_{l2} = 6Ω
Switch on-time T_{on}	--	10 μs

oscillator. The oscillator generates fixed duty cycle pulses to drive the flyback converter. Note that the oscillator does not perform dynamic resistive matching. When the supercapacitor is sufficiently charged, the MCU takes over the pulse generation and performs dynamic resistive matching, while the oscillator is shut off to save power. Since the average current dissipated by the MCU is approximately an order of magnitude higher than the oscillator, the MCU is active only when the piezoelectric harvester generates sufficient power to benefit from the dynamic resistive matching. More specifically, the MCU operates only when 1) the rectified voltage of the piezoelectric harvester is higher than a threshold voltage level, which is detected by Level Detector 1 in Fig. 6; and 2) the output voltage reaches a pre-determined level, which is detected by Level Detector 2. The decision to operate the oscillator or MCU is elaborated in the following.

Dynamic resistive matching increases the efficiency at the cost of higher power dissipation of the MCU compared with the oscillator. Therefore, dynamic resistive matching should be performed only when the net power harvested increases. Assume that the source impedance of the piezoelectric harvester is pure resistive and its value R_i is in the range of $[R_{s\min}, R_{s\max}]$. The switching frequency and the duty cycle of the oscillator are set accordingly, so that the input resistance of the flyback converter is equal to the midpoint of the two source resistances, i.e.,

$$R_{s\mathrm{mid}} = \frac{R_{s\min} + R_{s\max}}{2}. \tag{20}$$

Noting the input voltage to the flyback converter is V_{rect}, the input power delivered to the flyback converter under the oscillator is

$$P_{\mathrm{in,OSC}} = \frac{V_{\mathrm{rect}}^2}{R_{s\mathrm{mid}}}. \tag{21}$$

Now, consider the input power delivered to the converter under the MCU. Since the current through the input resistance $R_{s\mathrm{mid}}$ is $(V_{\mathrm{rect}}/R_{s\mathrm{mid}})$, the source voltage V_s is readily obtained as

$$V_s = \left(\frac{V_{\mathrm{rect}}}{R_{s\mathrm{mid}}}\right) R_i + V_{\mathrm{rect}}. \tag{22}$$

The MCU matches its input resistance to the source resistance R_i, and the power $P_{\mathrm{in,MCU}}$ delivered to the flyback converter is

obtained as follows:

$$P_{\mathrm{in,MCU}} = \frac{1}{4R_i} \left[\left(\frac{V_{\mathrm{rect}}}{R_{s\mathrm{mid}}}\right) R_i + V_{\mathrm{rect}} \right]^2. \tag{23}$$

Now, let us consider the power dissipation. The oscillator is powered up by the input voltage V_{rect}, while the MCU powered up by the output voltage V_o. (Refer to Figs. 6 and 7.) Hence, the total system loss under the oscillator and under the MCU is given as follows:

$$P_{\mathrm{loss,OSC}} = P_{\mathrm{loss,ps}} \left(V_{\mathrm{rect}}, R_{s\mathrm{mid}}\right) + V_{\mathrm{rect}} I_{\mathrm{OSC}} \tag{24}$$

$$P_{\mathrm{loss,MCU}} = P_{\mathrm{loss,ps}} \left(\frac{1}{2} \left[\left(\frac{V_{\mathrm{rect}}}{R_{s\mathrm{mid}}}\right) R_i + V_{\mathrm{rect}} \right], R_i \right)$$
$$+ V_o I_{\mathrm{MCU}} \tag{25}$$

where $P_{\mathrm{loss,ps}}$ denotes the power dissipated by the power stage as elaborated in the previous section, which is a function of the converter input voltage and the equivalent input resistance. I_{OSC} and I_{MCU} denote the current through the oscillator and the MCU, respectively. The MCU operates only if the net power harvested is greater than the net power harvested under the oscillator, which is expressed as follows:

$$\left(P_{\mathrm{in,MCU}} - P_{\mathrm{loss,MCU}}\right) > \left(P_{\mathrm{in,OSC}} - P_{\mathrm{loss,OSC}}\right). \tag{26}$$

If the rectifier output voltage V_{rect} is greater than a predetermined threshold voltage $V_{\mathrm{rect,th}}$, the aforementioned condition can be met.

IV. EXPERIMENTAL RESULTS

To verify the feasibility and measure the performance of the proposed PM system, we prototyped the system and experimented it with the aforementioned piezoelectric generator. Experimental results are presented in this section.

A. Prototyping and Experimental Setup

Based on the loss analysis described in the previous section, circuit parameters are judiciously chosen to minimize the loss of components. The circuit parameters for our system are listed in Table II and the prototyped circuit board is shown in Fig. 11.
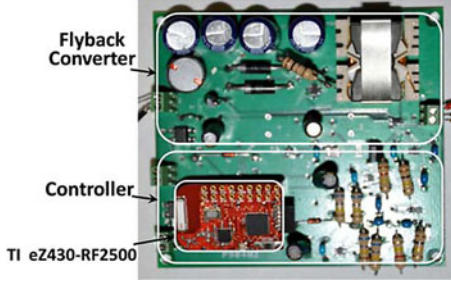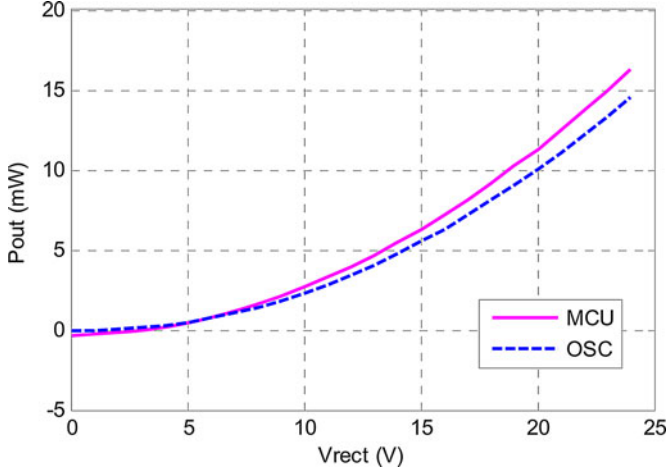
Fig. 11. Prototype of our system.

Fig. 12. Predicted power output of the system under different rectified voltage.

B. Start-Up and MPPT

The optimal resistive load ranges from 10 to 50 kΩ as shown in Fig. 5. The midpoint value is 30 kΩ, which is the target value set for the oscillator. The average current of the oscillator circuit I_{osc} is measured as 50 μA. According to the start-up strategy described in Section III-E, the potential power output driven by the oscillator and the MCU performing MPPT is calculated and plotted in Fig. 12. If the voltage after the rectifier is higher than 5 V, switching to the MCU generates more power. Therefore, the threshold rectified voltage $V_{\text{rect,th}}$ is set to 5 V.

Fig. 13 shows a transient response during a switch over from the oscillator to the MCU, while the supercapacitor is being charged up. Initially, the input voltage v_{rect} is around 13 V, which is above the threshold voltage $V_{\text{rect,th}} = 5$ V. When the supercapacitor voltage reaches above 3 V, the MCU takes over the control at 46 s as shown in Fig. 13(a). The transition from the oscillator to the MCU is also captured as shown in Fig. 13(b). To illustrate the transition, the initial off-time generated by the MCU is intentionally configured much higher than that of the oscillator for this experiment. Due to the abrupt increase of the off-time, the rectified voltage v_{rect} increases abruptly, while the input power P_{in} drops accordingly. As the MCU executes the MPPT algorithm, the input power increases steadily and reaches the peak at around 120 s. The rectified voltage decreases accordingly during the period and oscillates as it reaches the steady state.

Fig. 14 shows the steady-state waveforms of the current sensing signal v_{sense}, switching node voltage v_{sw}, charging current i_{charge}, and the gate drive signal v_{gs}. The waveforms in Fig. 14 match the DCM operation of a flyback converter depicted in Fig. 8. Note that when the diode current reduces to zero, the switching node voltage (the second one from top) rings due to the oscillation of the magnetizing inductance and the output capacitance of the MOSFET.

Next, we examine the performance of the MPPT algorithm executed by the MCU. We measured the on-time of the MOS-FET after the flyback converter reached the steady state, and calculated the equivalent input resistance of the converter using (3). The equivalent input resistance was compared with the optimal resistor load obtained manually. Fig. 15 shows the comparison of the two resistances for the frequency range of interest. The graphs show that the equivalent input resistance obtained by the MPPT algorithm is ±3 kΩ off the optimal resistor load. So, the MPPT algorithm executed by the MCU achieves good performance.

C. Efficiency

We measured the power output of the proposed PM system and compared it against that obtained by the optimal resistive load under 0.5-g base acceleration. The harvested power P_{out} on the supercapacitor delivered by our system and the maximal power P_{max} delivered to the optimal load are shown in Fig. 16. The maximal power P_{max} is about 11.9 mW at the resonant frequency of 47 Hz, and the harvested power P_{out} is 8.4 mW yielding the overall system efficiency η_{overall} of 70%. The maximal power P_{max} decreases rapidly as the vibration frequency moves away from the resonant frequency and, hence, harvested power P_{out} of the system. The harvested power ranges from 1.4 to 8.4 mW for the frequency range of 44 to 53 Hz, and the overall efficiency η_{overall} remains from 62% to 72%.

We are interested in the impact of the MPPT and the component loss to the overall efficiency, or MPPT efficiency η_{MPPT} and conversion efficiency $\eta_{\text{conversion}}$. (Refer to Section III-D for definitions of the efficiency.) The MPPT efficiency, the estimated and measured conversion efficiency, and the overall system efficiency are shown in Fig. 17. The MPPT efficiency stays above 94% for the entire frequency range of interest. High MPPT efficiency is expected, as the equivalent input resistance is close to the optimal one as shown in Fig. 15. The conversion efficiency stays in the range of 65% to 76% for the frequency range, and it is clear that the conversion dictates the overall system efficiency. The loss in the flyback converter is a function of the input voltage and input resistance. Substituting the measured input voltage and input resistance, we estimated the loss in the flyback converter, as well as the conversion efficiency. The discrepancy of the estimated efficiency and measured efficiency is less than 5%, which is possibly caused by the parasitic in the prototype. It implies that the loss analysis is relatively accurate and the reduction of power loss for components is essential to improve the system performance.
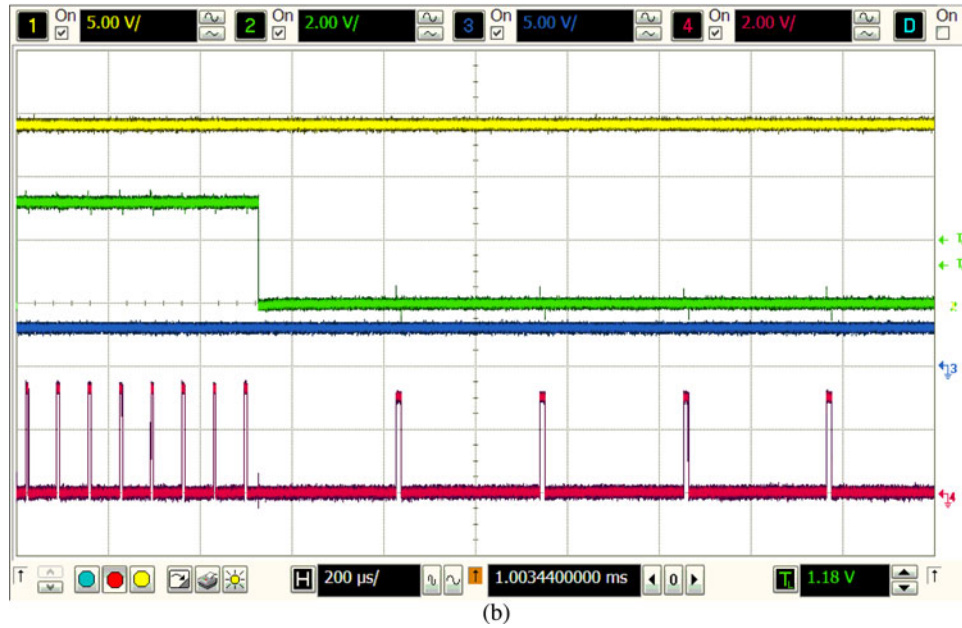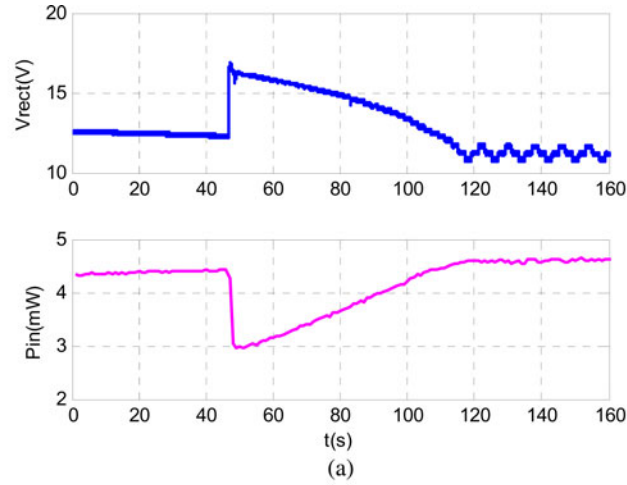
Fig. 13. Transient response during the switch over from the oscillator to the MCU. (a) Rectified voltage $V_{\rm rect}$ and converter input power $P_{\rm in}$. (b) Ch1: rectified voltage $v_{\rm rect}$, 5 V/div; Ch2: controller selection signal $v_{\rm ctrl\_sel}$, 2 V/div; Ch3: converter output voltage v_o, 5 V/div; Ch4: gate drive signal $v_{\rm gs}$, 2 V/div; 200 μs/div.)
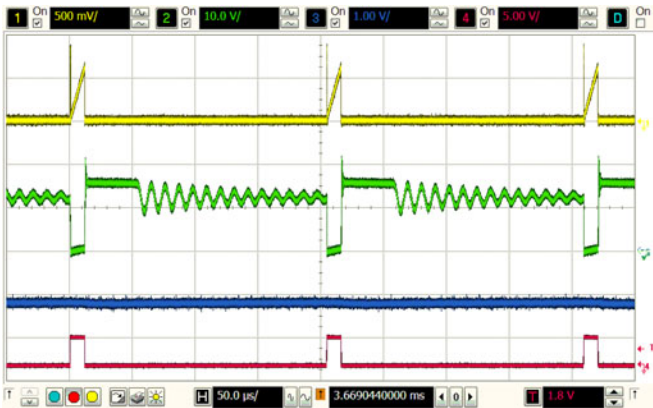

Fig. 14. Steady-state waveforms. (Ch1: current sensing signal $v_{\rm sense}$, 500 mV/div; Ch2: switching node voltage $v_{\rm sw}$, 10 V/div; Ch3: charging current $i_{\rm charge}$, 1 mA/div; Ch4: gate drive signal $v_{\rm gs}$, 5 V/div; 50 μs/div.)

D. Breakdown of the Losses

As indicated previously, the power loss of the components is the critical factor for the system efficiency. Fig. 18 shows the loss breakdown at the resonant frequency of 47 Hz. The diode D_F and the controller (specifically the MCU) are the major sources and account for 45% and 18% of the total power loss, respectively. The power loss of the diode is mostly the conduction loss, and a synchronous rectifier can be used to reduce the conduction loss at the cost of increased circuit complexity. The power consumption of the controller is 408 μW, which is a small fraction compared to the controller in [19], i.e., 5.74 mW. The power dissipation can be further reduced by setting a longer sleep time for the MCU at the cost of lower MPPT tracking speed.
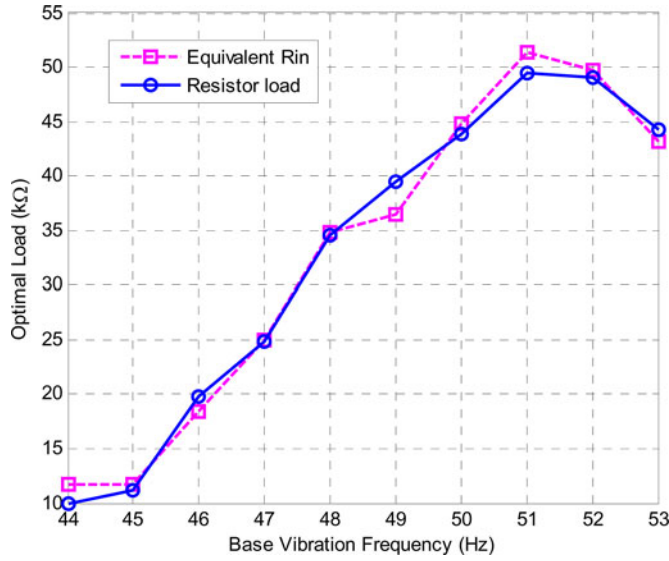
Fig. 15. Comparison of the equivalent input resistance of the flyback converter obtained through the MPPT and the optimal resistor.
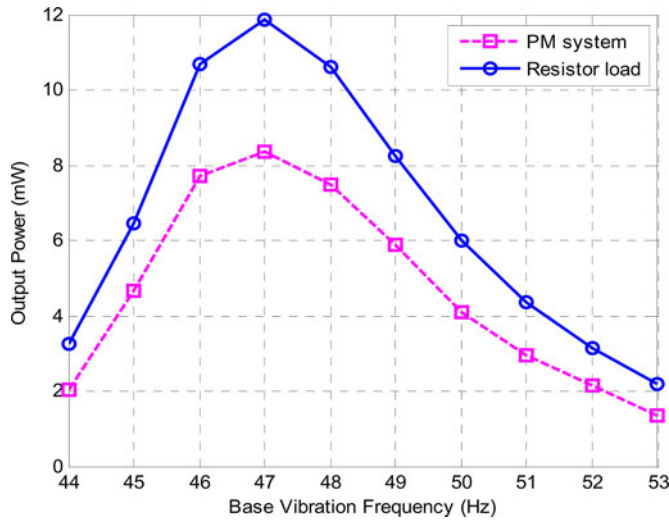

Fig. 16. Maximal power delivered by the piezoelectric generator and power harvested by the proposed system.

Fig. 17. MPPT, conversion, and system overall efficiency.

Fig. 18. Breakdown of the power loss.

E. Comparison With Other Systems

Although a direct and fair comparison with other competing systems is difficult because of the different target power and operating environments, it may be worth comparing our system with the system reported by Lefeuvre *et al*. [21]. Both systems adopt resistive matching and are self-powered, but Lefeuvre's system does not employ dynamic impedance or resistive matching. In spite of the adoption of dynamic resistive matching for our system, both systems achieve similar efficiency of about 70% at the same acceleration level. However, as the operating environment changes, it is expected that the efficiency of Lefeuvre's system would decrease rapidly due to the absence of dynamic impedance matching.
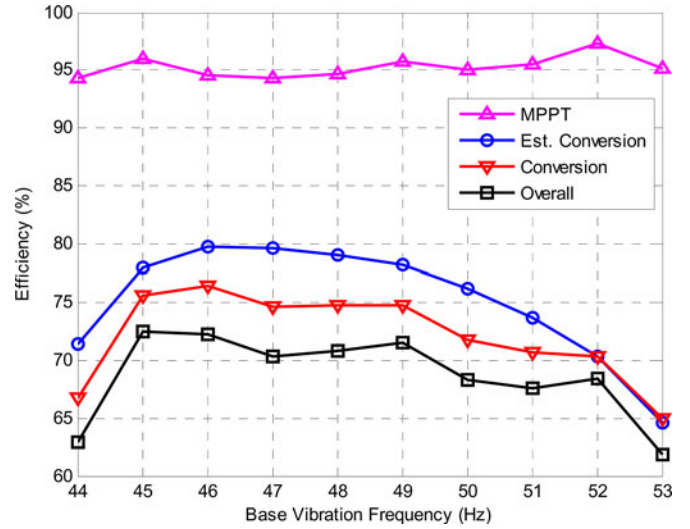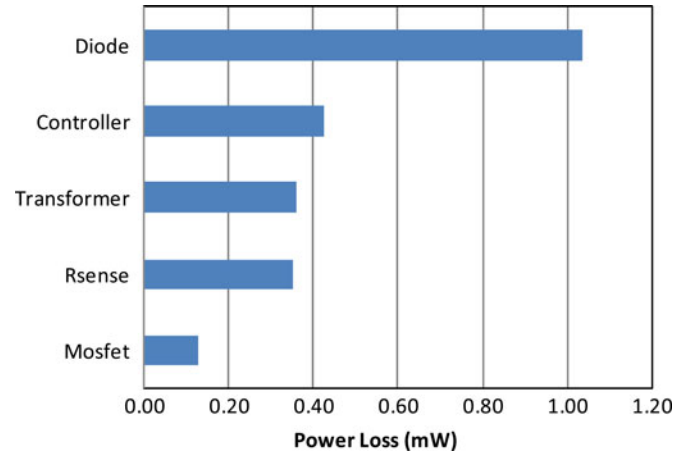
V. Conclusion

A low-power design of a piezoelectric energy harvesting system is presented in this paper. Several schemes to reduce power dissipation of the system are described, and sources of the power loss are analyzed. A DCM flyback converter with the constant on-time modulation is adopted for our system to realize dynamic resistive matching. The constant on-time modulation reduces the required clock frequency of the MCU, which reduces the power consumption. A low-power oscillator is adopted for our system to allow cold start.

Experimental results indicate that the proposed system harvests up to 8.4 mW of power under 0.5-g base acceleration using four parallel piezoelectric cantilevers and achieves 72% of the efficiency around the resonant frequency. The sources of the power loss are analyzed, and a breakdown of measured power loss is presented. The diode and the controller (specifically the MCU) are the two major sources for the power loss and account for 63% of the total power loss of the system. A synchronous rectifier can be used to reduce the diode conduction loss at the cost of increased circuit complexity. With a larger

number of piezoelectric cantilevers connected or under higher base acceleration, the efficiency of the proposed system will increase since the power dissipation of the controller circuit will not scale up. Future works include further improvement of the system efficiency and development of an efficient PM system in a monolithic IC. Finally, the circuit topology and low-power design schemes adopted for our system can be applied to other energy harvesting systems such as small-scale wind turbines and solar panels in a straightforward manner.

REFERENCES

[1] R. J. M. Vullers, R. V. Schaijk, H. J. Visser, J. Penders, and C. V. Hoof, "Energy harvesting for autonomous wireless sensor networks," *IEEE Solid-State Circuits Mag.*, vol. 2, no. 2, pp. 29–38, Spring 2010.

[2] Y. K. Tan and S. K. Panda, "Optimized wind energy harvesting system using resistance emulator and active rectifier for wireless sensor nodes," *IEEE Trans. Power Electron.*, vol. 26, no. 1, pp. 38–50, Jan. 2011.

[3] S. Dwari and L. Parsa, "An efficient AC–DC step-up converter for low-voltage energy harvesting," *IEEE Trans. Power Electron.*, vol. 25, no. 8, pp. 2188–2199, Aug. 2010.

[4] M. Lallart and D. J. Inman, "Low-cost integrable tuning-free converter for piezoelectric energy harvesting optimization," *IEEE Trans. Power Electron.*, vol. 25, no. 7, pp. 1811–1819, Jul. 2010.

[5] T. Paing, J. Shin, R. Zane, and Z. Popovic, "Resistor emulation approach to low-power RF energy harvesting," *IEEE Trans. Power Electron.*, vol. 23, no. 3, pp. 1494–1501, May 2008.

[6] H. Lhermet, C. Condemine, M. Plissonnier, R. Salot, P. Audebert, and M. Rosset, "Efficient power management circuit: From thermal energy harvesting to above-IC microbattery energy storage," *IEEE J. Solid-State Circuits*, vol. 43, no. 1, pp. 246–255, Jan. 2008.

[7] C. Alippi and C. Galperti, "An adaptive system for optimal solar energy harvesting in wireless sensor network nodes," *IEEE Trans. Circuits Syst. I, Reg. Papers*, vol. 55, no. 6, pp. 1742–1750, Jul. 2008.

[8] S. R. Anton and H. A. Sodano, "A review of power harvesting using piezoelectric materials (2003–2006)," *Smart Mater. Struct.*, vol. 16, pp. R1–R21, 2007.

[9] S. P. Beeby, M. J. Tudor, and N. M. White, "Energy harvesting vibration sources for microsystems applications," *Meas. Sci. Technol.*, vol. 17, pp. 175–195, 2006.

[10] S. Roundy, E. S. Leland, J. Baker, E. Carleton, E. Reilly, E. Lai, B. Otis, J. M. Rabaey, P. K. Wright, and V. Sundararajan, "Improving power output for vibration-based energy scavengers," *IEEE Pervasive Comput.*, vol. 4, no. 1, pp. 28–36, Mar. 2005.

[11] C. Richard, D. Guyomar, D. Audigier, and G. Ching, "Semi-passive damping using continuous switching of a piezoelectric device," in *Proc. SPIE*, 1999, vol. 3672, pp. 104–111.

[12] D. Guyomar, A. Badel, E. Lefeuvre, and C. Richard, "Toward energy harvesting using active materials and conversion improvement by nonlinear processing," *IEEE Trans. Ultrason., Ferroelectr., Freq. Control*, vol. 52, no. 4, pp. 584–595, Apr. 2005.

[13] A. B. A. Badel, E. Lefeuvre, L. Lebrun, C. Richard, and D. Guyomar, "Single crystals and nonlinear process for outstanding vibration-powered electrical generators," *IEEE Trans. Ultrason., Ferroelectr., Freq. Control*, vol. 53, no. 4, pp. 673–684, Apr. 2006.

[14] S. Xu, K. D. T. Ngo, T. Nishida, G.-B. Chung, and A. Sharma, "Low frequency pulsed resonant converter for energy harvesting," *IEEE Trans. Power Electron.*, vol. 22, no. 1, pp. 63–68, Jan. 2007.

[15] M. Lallart and D. Guyomar, "An optimized self-powered switching circuit for non-linear energy harvesting with low voltage output," *Smart Mater. Struct.*, vol. 17, pp. 035030 (8 pp.), 2008.

[16] J. Liang and W.-H. Liao, "An improved self-powered switching interface for piezoelectric energy harvesting," in *Proc. IEEE Int. Conf. Inf. Autom.*, 2009, pp. 945–950.

[17] Y. K. Ramadass and A. P. Chandrakasan, "An efficient piezoelectric energy harvesting interface circuit using a bias-flip rectifier and shared inductor," *IEEE J. Solid-State Circuits*, vol. 45, no. 1, pp. 189–204, Jan. 2010.

[18] G. K. Ottman, H. F. Hofmann, A. C. Bhatt, and G. A. Lesieutre, "Adaptive piezoelectric energy harvesting circuit for wireless remote power supply," *IEEE Trans. Power Electron.*, vol. 17, no. 5, pp. 669–676, Sep. 2002.

[19] G. K. Ottman, H. F. Hofmann, and G. A. Lesieutre, "Optimized piezoelectric energy harvesting circuit using step-down converter in discontinuous conduction mode," *IEEE Trans. Power Electron.*, vol. 18, no. 2, pp. 696–703, Mar. 2003.

[20] A. Kasyap, J. Lim, D. Johnson, S. Horowitz, T. Nishida, K. Ngo, M. Sheplak, and L. Cattafesta, "Energy reclamation from a vibrating piezoceramic composite beam", presented at the 9th Int. Congr. Sound Vibration, Orlando, FL, 2002, Paper 271.

[21] E. Lefeuvre, D. Audigier, C. Richard, and D. Guyomar, "Buck-boost converter for sensorless power optimization of piezoelectric energy harvester," *IEEE Trans. Power Electron.*, vol. 22, no. 5, pp. 2018–2025, Sep. 2007.

[22] N. Kong, D. S. Ha, A. Erturk, and D. J. Inman, "Resistive impedance matching circuit for piezoelectric energy harvesting," *J. Intell. Mater. Syst. Struct.*, vol. 21, pp. 1293–1302, 2010.

[23] A. Tabesh and L. G. Frechette, "A low-power stand-alone adaptive circuit for harvesting energy from a piezoelectric micropower generator," *IEEE Trans. Ind. Electron.*, vol. 57, no. 3, pp. 840–849, Mar. 2010.

[24] Sam, N. Kong, T. Cochran, H. Dong, L. Hung-Chih, and D. J. Inman, "A self-powered power management circuit for energy harvested by a piezoelectric cantilever," in *Proc. IEEE Appl. Power Electron. Conf. Expo.*, Palm Springs, CA, 2010, pp. 2154–2160.

[25] D. Kwon and G. A. Rincon-Mora, "A single-inductor AC–DC piezoelectric energy-harvester/battery-charger IC converting (0.35 to 1.2 V) to (2.7 to 4.5 V)," in *Proc. IEEE Int. Solid-State Circuits Conf.*, San Francisco, CA, 2010, pp. 494–495.

[26] N. G. Elvin and A. A. Elvin, "A general equivalent circuit model for piezoelectric generators," *J. Intell. Mater. Syst. Struct.*, vol. 20, pp. 3–9, 2009.

[27] A. Erturk and D. J. Inman, "An experimentally validated bimorph cantilever model for piezoelectric energy harvesting from base excitations," *Smart Mater. Struct.*, vol. 18, pp. 025009 (18 pp.), 2009.

[28] W. Erickson and D. Maksimovic, *Fundamentals of Power Electronics*. Norwell, MA: Kluwer, 2001.

[29] J. Li, Y. Qiu, Y. Sun, B. Huang, M. Xu, D. S. Ha, and F. C. Lee, "High resolution digital duty cycle modulation schemes for voltage regulators," in *Proc. IEEE Appl. Power Electron. Conf. Expo.*, Feb. 2007, pp. 871–876.

[30] T. Esram and P. L. Chapman, "Comparison of photovoltaic array maximum power point tracking techniques," *IEEE Trans. Energy Convers.*, vol. 22, no. 2, pp. 439–449, Jun. 2007.

[31] N. Femia, G. Petrone, G. Spagnuolo, and M. Vitelli, "Optimization of perturb and observe maximum power point tracking method," *IEEE Trans. Power Electron.*, vol. 20, no. 4, pp. 963–973, Jul. 2005.
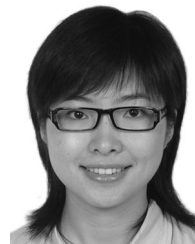
Na Kong (S'08) received the B.S. and M.S. degrees in biomedical engineering from Tsinghua University, Beijing, China, in 2004 and 2006, respectively, and the Ph.D. degree in computer engineering from Virginia Tech, Blacksburg, Virginia, in 2011.

Her main research interests include power management circuit design for energy harvesting and digital control for switched-mode power supplies.

Dong Sam Ha (M'86–SM'97–F'08) received the B.S. degree in electrical engineering from Seoul National University, Seoul, Korea, in 1974, and the M.S. and Ph.D. degrees in electrical and computer engineering from the University of Iowa, Iowa City, in 1984 and 1986, respectively.

Prior to his graduation, he was with the Agency for Defense Development, Daejeon, Korea, for five years. Since Fall 1986, he has been a faculty member of the Bradley Department of Electrical and Computer Engineering, Virginia Tech, where he is currently a Professor. His group has developed four computer-aided design tools for digital circuit testing and CMOS standard cell libraries. The source code for the four tools and the cell libraries have been distributed to more than 300 universities and research institutions worldwide. His group specializes in low-power design for digital, analog/mixed-signal, and RF ICs targeting for embedded system applications. His research interests include power conditioning circuits for energy harvesting, structural health monitoring systems and processors, and high temperature RF ICs.

Dr. Ha was the General Chair of the System-on-Chip Conference in 2005 and the Technical Program Chair of the System-on-Chip Conference in 2003 and 2004.